ANALYSIS OF MICROSEISMIC LOCATION ACCURACY FOR HYDRAULIC FRACTURING AT THE DWTI SITE, JASPER, TEXAS

Shirley Rieven and William Rodi

Earth Resources Laboratory
Department of Earth, Atmospheric, and Planetary Sciences
Massachusetts Institute of Technology
Cambridge, MA 02139

ABSTRACT

This report presents the results of a feasibility study designed to assess whether microseismic location techniques can provide enough accuracy and precision to enable a high resolution study of the spatial distribution of microseismic events induced during a hydraulic fracture experiment. We calculated the 90% confidence regions for six synthetic microevent 'clusters' along the azimuth of a hydraulic fracture produced during Atlantic Richfield's 1993 Fracture Technology Field Demonstration Project in Jasper, Texas. Examination of the confidence regions for the absolute locations indicates that microseismic events can be confidently located for areas near the monitoring wells but away from the plane intersecting the two observation points. We determined that the resolution for events located at the ends of the fracture is poor but improves dramatically nearer the wells. The minimum dimensions of the 90% confidence regions for events within our study area are approximately 8 ft in the northwest-southeast direction, 3 ft in the northeast-southwest direction, and 3 ft in depth.

INTRODUCTION

Delineating the spatial distribution of hydraulically-induced fractures has been the subject of active research for over twenty years, particularly as it applies to exploration for oil, natural gas and geothermal energy resources. Recovery of resources from a reservoir may require stimulation of these fractures, therefore a thorough understanding of their interaction is crucial to an effective design. The methods used to determine the basic fracture parameters of height, azimuth and width have evolved over the years and have

included such disparate techniques as shear acoustic anisotropy, anelastic strain recovery (ASR), overcoring of microfracs, natural and coring induced core fractures, borehole microseismic monitoring, and borehole televiewer imaging. Microseismic monitoring is unique among these techniques in that it is the only method capable of resolving, in a non-invasive manner, the macroscopic three-dimensional structure of the fracture at significant distances from the borehole. This method is not vulnerable to disturbances associated with core recovery (a particular problem in unconsolidated materials) and has been shown to compare favorably in accuracy to several of the best methods, specifically ASR, and overcoring (Yale *et al.*, 1992). The emergence of advanced sensor technology for microboreholes will impact the cost/benefit of this method bringing it into a more favorable position with respect to the alternative techniques. This development presents a unique opportunity to more clearly determine the parameters governing the shape of hydraulic fractures under field conditions and to improve our confidence in the hypocenter locations derived from the associated induced microseismicity.

A variety of methods have been used to determine the hypocentral location coordinates and origin times of microseismic events induced by hydraulic fracturing. Prior to the early 1980s, the hypocenters and origin times were commonly determined using variations of Geiger's method and alternatively, the 3-point method originally introduced by Lutz in 1986 (Fehler *et al.*, 1987). Later developments incorporated the use of relative event location techniques to locate microearthquakes that are closely placed in space. These techniques were later expanded to include the use of cross-spectral, moving-window methods to make use of the similarity of related events called doublets (Frechet *et al.*, 1989; Frankel, 1982; Geller and Mueller, 1980; Poupinet *et al.*, 1984; Thornjarnardottir and Pechmann, 1987; Fremont and Malone, 1987; Deichmann and Garcia-Fernandez, 1992; Moriya *et al.*, 1994).

This paper presents an evaluation of the microseismic location accuracy for a solid waste disposal demonstration project conducted by Atlantic Richfield Corporation. The microseismic activity was monitored using 150 downhole geophones, making this experiment one of the most heavily instrumented to date. This high receiver density presents an excellent opportunity to study the fracturing process in greater detail than has been attempted using data from sparser arrays. We are particularly interested in the occurrence of seismicity away from the plane of the fracture. Traditional treatment of the hydraulic fracture process predicts rupture along a planar fracture due to tensile effective stresses, yet, past seismic monitoring of hydrofracture experiments have suggested the occurrence of microseismicity away from the predicted plane. Our immediate goal is to determine whether the accuracy of our location technique is sufficient to investigate these remote rupture processes. We begin by assessing our location algorithm's ability to spatially resolve the hypocenters. To this end, we determined the 90% confidence regions for 6 grids of synthetic hypocenters by forward modeling the P and S wave traveltimes to the known locations of the seismic receivers used in the demonstration. We synthesized picking errors by adding distance-weighted random noise and then inverting for the absolute hypocenter parameters. We used this procedure to evaluate the lateral

variation of the confidence regions so as to quantify the maximum resolution attainable from the DWTI data.

THE FRACTURE TECHNIQUES TECHNOLOGY FIELD DEMONSTRATION PROJECT

Atlantic Richfield's Deep Well Treatment and Injection Program

Atlantic Richfield Corporation (ARCO) proposed that solid waste could be safely disposed of by suspending the solids in a bentonite slurry and injecting them into deeply buried, hydrogeologically isolated formations. ARCO presented the method and its safe application in a Fracture Technology Field Demonstration conducted over a five day period in October 1993 at the Deep Well Treatment and Injection Site (DWTI) in Jasper, Texas (Figure 1). During the demonstration, ARCO injected 4 million pounds of sand and bentonite clay and 2.1 million gallons of water into an isolated portion of the Lower Frio Sand. The injection was conducted in four segments designated as cycles 0, 1, 2, and 3. These injection cycles hydraulically fractured the sand while forcing the sand/clay suspension into the fractured zone and surrounding formation. The demonstration specifically addressed two key issues concerning the disposal method: (1) the technique must be able to dispose of a significant quantity of waste; and (2) the zone of disposal must be known to ensure containment of the wastes within the isolated formation. The answer to the first issue was given immediately by the amount of simulated waste injected during the demonstration. The second issue was addressed in two parts. First, ARCO showed that the fracture growth could be monitored in real time by locating microseismic events induced by the fracture. Second, they demonstrated that the fracture dimensions determined by microseismic monitoring were in agreement with those predicted by currently available fracture modeling methods and that the results from both methods suggested that the fracture had not compromised the integrity of the confining layers (Atlantic Richfield Corporation, 1994).

Geologic Environment

ARCO produced the DWTI hydraulic fracture by injecting the simulated waste into an isolated sand layer via a well designated the Field Technology Demonstration Well #2 (FTD #2). Simultaneously, microseismic events were recorded by geophones located in two monitoring wells designated FTD Wells #1 and #3. Figure 2 shows the field geometry of the three wells. The injection well (FTD #2) was constructed using standard petroleum field completion with the perforation extending from 4426–4614 ft. ARCO placed the perforation so that the geologic unit receiving the waste was a 155 ft thick portion of the Lower Frio Sand (Figure 3). This section of the Lower Frio Sand is bounded above by a 130 ft thick layer of shale and below by a 1500 ft thick layer of shale. The Lower Frio Sand is regionally continuous and of large lateral extent. The nearest known fault is at a distance of 5000 ft away from the perforated zone (ARCO,

1994). The perforation extends slightly below the top of the lower bounding shale, but due to the very large vertical extent of this unit, the slight intrusion did not pose a difficulty for the disposal demonstration.

Seismic Receiver Geometry

ARCO placed 150 30-Hertz geophones in the two monitoring wells to record the microseismic activity during the injection. Two strings of 75 geophones (25 pods, each containing three orthogonally-oriented phones) were installed—one string in each of the two monitoring wells (FTD #1 and #3). The 25 pods were located along the strings at 30 ft intervals over a range spanning the target sand layer and portions of the upper and lower bounding shales. The full string of phones provided a total aperture of 720 ft for each well (Figure 3). ARCO located each pod vertically by radioactive tracers, but the absolute orientation of the two horizontal phones in each pod has not been determined. The Frio Sand is a permeable, unconsolidated layer prone to washouts; therefore, the geophone strings were cemented inside the casings. The microseismic activity was sampled continuously at a rate of 2000 samples per second and detected events were isolated and saved as separate event files. Approximately 2400 individual events were recorded during the five-day demonstration.

ARCO chose the lateral location of the monitoring wells based upon the predicted azimuth of the fracture as determined from various lab and field experiments. Hydraulic fractures, induced at depth from non-deviated wellbores, propagate perpendicular to the direction of least principal stress. Therefore, three separate laboratory tests were conducted on cores from FTD Well #1 to determine this direction. These tests included Anelastic Strain Recovery (ASR), Differential Strain Curve Analysis (DSCA), and Velocity Anisotropy (VELAN). ASR predicted the least principal stress as being N35E $\pm$ 5°, DSCA predicted the direction to be N12E to N40E, and VELAN predicted the direction to be N35E $\pm$ 5°. Televiewer inspection of borehole breakouts indicated a minimum stress direction of N45E $\pm$ 30°, while examination of the strikes of nearby growth faults indicated that the regional minimum stress direction was N80E $\pm$ 20°. Because of the amount of disagreement between these estimates, ARCO conducted a microfrac test (fracture azimuth injection test). The azimuth of the fracture induced during this test was monitored using a surface array of tiltmeters (Figure 2). The final estimate of fracture azimuth was taken to be N40E. Based upon a combination of these test results, the monitoring wells were installed such that the expected azimuth of the fracture bisected both wells. Despite the preliminary estimates, the DWTI fracture propagated N66E and thus did not bisect the two monitoring wells as expected. Due to the nature of the experiment and the large lateral extent of the Lower Frio Sand unit, the unexpected fracture azimuth had little effect on the objective of the demonstration. These difficulties, however, illustrate the difficulty in determining accurate fracture propagation parameters.

DWTI Fracture Geometry

During the hydraulic fracturing, microseismicity was recorded by 96 of the 150 available geophones via ARCO's Digital Acquisition System. In addition to being saved as an independent file, each detected event was examined to determine which geophone along the string triggered first. Based upon the vertical receiver geometry and the concept of minimum traveltime, a preliminary estimate of the hypocentral depth was determined. This method allowed a real-time assessment of vertical fracture growth, accurate to one-half of the pod spacing (15 ft) which was accurate enough (relative to the vertical extent of the bounding shale layers) to determine whether the microseismicity was confined within the sand layer (as predicted by the mathematical fracture algorithms). The real time estimates were suggested that the fracture had, indeed, stayed within the target zone, and this assessment was further supported by subsequent, more precise locations determined for the 100 largest magnitude events using an inversion algorithm developed by Los Alamos National Laboratory (House, 1987). Figures 4 and 5 show the epicentral and depth locations of these 100 events (as located by ARCO).

FORWARD MODELING OF SYNTHETIC MICROEVENT CLUSTERS

The objective of this study was to assess the lateral variation of the 90% confidence regions for the hypocenters of hypothetical (synthetic) microearthquake clusters located along the azimuth of the DWTI hydraulic fracture. Figures 6 and 7 show six synthetic event clusters with two different inter-event spacings—50 ft and 100 ft—upon which we conducted our numerical experiments. In the following sections we present the method used to calculate the hypocenter coordinates and the results of the accuracy and spatial variation tests.

Method for Determining Hypocenter Location

Our event relocation method fits the hypocenters and origin times of a set of events in a cluster simultaneous to a set of absolute and differential arrival time data observed at various stations. The absolute arrival time for an event e, station s and wave type w (P or S) is modeled as

$$T_{esw} = t_e + F(x_e, x_s, u_w) + n_{esw}. \tag{1}$$

Here, x_e is the hypocentral coordinate vector and t_e the origin time of the event. The function F gives the theoretical traveltime between x_e and the station location x_s through an assumed slowness model u_w. n_{esw} denotes the observational error in T_{esw}. Differential arrival times between a "slave" event e and a "master" event r are modeled as

$$\Delta T_{resw} = t_e - t_r + F(x_e, x_s, u_w) - F(x_r, x_s, u_w) + n_{resw}. \tag{2}$$

Note that the observational error in a differential time is not a difference between absolute arrival time errors, because we assume that ΔT_{resw} has been measured independently of T_{esw} and T_{rsw}. An additional source of error occurs in both absolute and differential times when the slowness models u_w are not known exactly, e.g., a one-dimensional approximate model is often assumed. Such "modeling errors" affect primarily absolute times and tend to cancel in differential times between closely spaced events. We solve equations (1) and (2) for the x_e and t_e, using available (e, s, w) and (r, e, s, w) combinations, by minimizing the errors n_{esw} and n_{resw} in a least squares sense using a conjugate gradient algorithm (Rodi *et al.*, 1993). Estimates of the errors in the predicted locations are determined using linear approximations and the statistical methods outlined by Jordan and Sverdrup (1981).

Forward Modeling of the P and S Wave Traveltimes With Noise

We calculated the P and S wave arrival times for the synthetic hypocenters shown in Figures 6 and 7 at a depth of 4500 ft, using a horizontally-layered velocity structure model with P wave velocities for the sand of 8100 ft/sec and S wave velocities of 3682.0 ft/sec. Shale P wave velocities were set to 7272.7 ft/sec, with shale S wave velocities of 3305.8 ft/sec. In calculating the arrival times, we specified picking error uncertainties derived from a linear dependence on horizontal distance between the hypocenter and the monitoring well. These errors were approximated by adding pseudo-random noise with a Gaussian distribution. We specified the standard deviations based upon ARCO's estimate of the picking error for the primacord shots (1 ms) and on RMS errors for previously located events in cycle 2 (located near the farthest extent of fracture propagation), 6 ms. Figure 8 shows the results of a test conducted to confirm the accuracy of the 90% confidence regions for one of the synthetic hypocenters from Grid Ab (event Abyy). This figure shows the predicted hypocenters determined using 60 independent sets of noise. Fifty-four of the 60 hypocenter estimates (93%) fall within the 90% confidence region, demonstrating that the regions calculated for this study are correct. (The confidence region presented for comparison is taken from the most accurate relocated event of the 60 studied).

We tested the accuracy of our hypocenter location algorithm by comparing the location of the 90% confidence regions with the true location of the hypocenters. The results of this study are presented beginning with the grid furthest southwest (Grid A) and progressing toward the northeast. With this ordering, the confidence ellipses begin large, pass through the expected minimum size, and then increase again as we exit the area best covered by the receiver geometry. The ellipses determined for grids A through E (at 50 ft spacing) are shown in Figures 9–14. The circles plotted represent the true locations of the hypocenters, whereas the estimated hypocenters are at the center of the 90% confidence regions as estimated by the inversion algorithm. Additionally, we included the location of real hypocenters from the DWTI (as located by ARCO) to indicate the relative spacing between actual events. The confidence regions for grids D, E and F (Figures 12, 13, and 14) illustrate the poor confidences possible for areas

northeast of the wells. No further consideration of events in grids D, E, or F will be given based upon these results.

The results from the forward modeling for grids Aa–Ea quantify the spatial variation in confidence regions over the length of the southwestern wing of the fracture (Figures 9, 10, and 11). The average maximum semi-axis for the events in this wing varies from a maximum of 55 ft (center of grid Aa) to 12 ft (center of grid Ca). The average minimum semi-axis for the events varies from a maximum of 11 ft (center of grid Aa) to 4 ft (center of grid Ca). The 90% confidence region for the depth axis varies from a maximum of 12 ft (center of grid Aa) to a minimum of 3 ft (center of grid Ca). All range values are rounded to the nearest foot. It is also apparent that the geometry of the wells contributes to the characteristics of the confidence regions. The average azimuthal direction of the major axis varies spatially from N21.3W (grid A) to N8.5E (grid B), a clockwise rotation around the wells. For grids A and B, the wells are both located on the eastern side. The azimuth changes to N37.8W for grid C, located longitudinally between the two wells.

We also calculated the regions for grids with 100 ft spacing to evaluate the lateral variation in region size and orientation (Figures 15, 16, and 17). The results of the inversions for the 100 ft grids are presented quantitatively in Table 1. Convergence was commonly attained within 11 iterations of the conjugate gradient algorithm with final RMS misfits and average posteriori standard deviations of approximately 1.00. These results show the variation in the major semi-axis of the confidence regions as a function of distance away from the line connecting the two monitoring wells. Li and Thurber (1991) demonstrated that for receiver arrays with only two laterally separated monitoring locations, the spatial resolution is poor for events along the plane separating the observation points. We can observe this effect for the DWTI data by comparing the semi-major axes diagonally across the grids. This axis dimension increases by a factor of 1.88 for grid A, far from the intersecting plane, but by a factor of 3.47 for grid C, nearest the intersecting plane. We also observe the effect of distance from the plane by inspecting the change in ellipse azimuth across the grid. Grid A shows a variation of approximately 12.3° (clockwise rotation) between event Abzz and Abxx. Variations of 36.9° and 4.9° (counterclockwise), are observed for grids B and C, respectively.

We can use the 90% confidence regions predicted for grids A through C to qualitatively determine the resolvability of events within the actual DWTI fracture zone, as determined from the events located by ARCO. It is clear from inspection of the semi-major axis dimensions for all three grids that the resolution in the northeast-southwest direction is good, especially for events located within the region covered by grid C. However, resolution of the hypocenter coordinates in the northwest-southeast direction varies considerably over the length of the extent of the fracture wing. Actual events from the early phases of the DWTI injection (cycle 1) were determined to be located within grid C (Figures 4, 6, and 7). These events are closely spaced but resolvable in many instances (Figures 16 and 17). The events induced during cycle 2 are less well-resolved, particularly in the northwest-southeast direction (Figure 15).

These results compare favorably with those found for other experiments of this type. For example, House (1987) located the hypocenters of 805 microseismic events at the Fenton Hill Geothermal Field using similar techniques. These events were located with an accuracy of 25 to 30 meters. Vinegar *et al.* (1992) estimated the accuracy of relative event location of events in a downhole experiment similar to the DWTI demonstration as being 1.5 ft radially and 1 ft vertically, but noted that absolute locations would be much greater.

CONCLUSIONS

The results of this study indicate that microseismic events induced by hydraulic fracturing during the Atlantic Richfield Corporation Field Demonstration Project can be confidently located for areas near the monitoring wells but away from the plane intersecting the two observation points. We determined that the minimum dimensions of the 90% confidence regions for events within our study area are approximately 8 ft in the northwest-southeast direction, 3 ft in the northeast-southwest direction, and 3 ft in depth.

The results of this study suggest that the resolution provided by the technique of absolute hypocenter location as it applies specifically to the Field Demonstration Experiment, are comparable to that found in other similar studies. However, we show that the area of good resolution excludes the extreme lateral extent of the fracture thus limiting the detail with which we can examine the fracture process. The location errors can be interpreted as the minimum distance between fractures that is resolvable using this technique. We anticipate that application of relative event location techniques to real data from the DWTI demonstration will improve the accuracy of the hypocenter locations by reducing the arrival time picking errors and minimizing any effects of erroneous velocity model estimates. An analysis of the expected improvement will further define the minimum fracture separation resolvable in those areas not adequately addressed using absolute location techniques.

ACKNOWLEDGMENTS

We would like to thank Dr. Robert Withers and Atlantic Richfield Corporation for providing the seismic data and project logistics information used to complete this preliminary study.

REFERENCES

Atlantic Richfield Corporation, The deep well treatment and injection program, Fracture Technology Field Demonstration Project, April, 1994.

Deichmann, N. and M. Garcia-Fernandez, Rupture geometry from high-precision relative hypocentre locations of microearthquake clusters, *Geophys. J. Int.,* 501–517, 1992.

Fehler, M., L. House, and H. Kaieda, Determining planes along which earthquakes occur: Method and application to earthquakes accompanying hydraulic fracturing, *J. Geophys. Res., 92,* 9,407–9,414, 1987.

Frankel, A., Precursors to a magnitude 4.8 earthquake in the Virgin Islands: Spatial clustering of small earthquakes, anomalous focal mechanisms, and earthquake doublets, *Bull. Seismol. Soc. Am., 72,* 1277–1294, 1982.

Frechet, J., L. Martel, L. Nikolla, and G. Poupinet, Application of the cross-spectral moving-window technique (CSMWT)to the seismic monitoring of forced fluid migration in a rock mass., *Internat. Journ. Rock Mech. and Mining Sci. and Geomechanics Abstracts, 26,* 221–233, 1989.

Fremont, M. and S. Malone, High precision relative locations of earthquakes at Mount Saint Helens, Washington, *J. Geophys. Res., 92,* 10,223–10,236, 1987.

Geller, R. and C. Mueller, Four similar earthquakes in central California, *Geophys. Res. Lett., 7,* 821–824, 1980.

House, L., Locating microearthquakes induced by hydraulic fracturing in crystalline rock, *Geophys. Res. Lett., 14,* 919–921, 1987.

Jordan, T. and K. Sverdrup, Teleseismic location techniques and their application to earthquake clusters in the south-central Pacific, *Bull. Seismol. Soc. Am., 71,* 1,105–1,130, 1981.

Li, Y. and C. H. Thurber, Hypocenter constraint with regional seismic data: A theoretical analysis for the natural resources defense council network in Kazakstan, USSR, *J. Geophys. Res.,* 10,159–10,176, 1991.

Moriya, H., K. Nagano, and H. Niitsuma, Precise source location of AE doublets by spectral matrix analysis of triaxial hodogram, *Geophysics, 59,* 36–45, 1994.

Poupinet, G., W. Ellsworth, and J. Frechet, Monitoring velocity variations in the crust using earthquakes doublets: An application to the Calaveras Fault, *J. Geophys. Res., 89,* 5,719–5,731, 1984.

Rodi, W., Y. Li, and C. Cheng, Location of microearthquakes induced by hydraulic fracturing, in *Borehole Acoustics and Logging Consortium Annual Report,* 369–410, Earth Resources Laboratory, Massachusetts Institute of Technology, 1993.

Thornjarnardottir, B. and J. Pechmann, Constraints on relative earthquake locations from cross-correlation of waveforms, *Bull. Seismol. Soc. Am., 77,* 1,626–1,634, 1987.

Vinegar, H., P. Wills, D. DeMartini, J. Shlyapobersky, W. Deeg, R. Adair, J. Woerpel, J. Fix, and G. Sorrells, Active and passive seismic imaging of a hydraulic fracture in diatomite, *J. Petrol. Tech., 44,* 1992.

Yale, D., M. Strubhar, and A. El Rabaa, A field comparison of techniques for determining the direction of hydraulic fractures, in *Proceedings of the 33rd U.S. Symposium on Rock Mechanics,* J. Tillerson and W. Wawersik (eds.), 89–98, 1992.

Event	Iterations	RMS Misfit	σ posteriori	Ellipse Strike	Major axis (ft)	Minor axis (ft)	Depth (ft)
Abxx	10	1.053	1.05	-14.8	45.93	11.59	13.37
Abxy	9	1.050	1.05	-14.2	39.99	11.50	12.00
Abxz	7	0.959	0.97	-17.4	37.87	10.52	9.92
Abyx	8	0.976	0.98	-20.2	58.26	10.71	12.75
Abyy	11	0.968	0.98	-21.3	55.90	10.61	11.48
Abyz	21	0.986	0.98	-25.1	66.87	10.75	10.50
Abzx	21	1.019	1.02	-26.3	98.25	11.20	13.73
Abzy	16	0.998	1.00	-26.8	92.37	10.91	12.27
Abzz	8	1.012	1.02	-27.1	86.50	11.04	11.27
Bbxx	6	1.051	1.05	5.0	12.43	7.06	5.53
Bbxy	5	1.050	1.05	7.1	10.20	7.16	4.79
Bbxz	5	0.961	0.97	2.6	7.82	6.77	3.84
Bbyx	6	0.975	0.98	-6.7	15.39	6.51	5.09
Bbyy	5	0.968	0.98	-8.5	13.58	6.51	4.36
Bbyz	6	0.986	0.99	-13.0	12.60	6.65	3.80
Bbzx	6	1.019	1.02	-18.4	26.10	6.72	5.40
Bbzy	8	0.996	1.00	-21.0	25.40	6.59	4.58
Bbzz	11	1.011	1.02	-25.2	28.11	6.65	4.01
Cbxx	6	1.053	1.05	-41.9	8.05	4.01	3.88
Cbxy	5	1.051	1.05	-33.2	8.94	3.73	3.75
Cbxz	6	0.955	0.97	-25.1	8.33	3.57	3.37
Cbyx	5	0.974	0.98	-46.3	8.57	3.38	3.25
Cbyy	5	0.970	0.98	-37.8	11.88	2.99	3.23
Cbyz	10	0.994	1.00	-32.3	17.27	3.02	3.33
Cbzx	5	1.019	1.02	-49.6	10.97	3.44	2.98
Cbzy	10	0.953	1.00	-39.6	25.35	2.86	3.04
Cbzz	16	1.011	1.02	-37.0	27.92	2.90	3.29
Dbxx	6	1.057	1.06	-54.9	24.65	8.09	6.51
Dbxy	10	1.050	1.05	-46.6	50.01	8.02	6.87
Dbxz	27	0.957	0.97	-45.3	59.59	7.41	6.89
Dbyx	11	0.974	0.98	-50.3	25.77	7.40	5.44
Dbyy	10	0.971	0.98	-43.3	61.80	7.40	5.87
Dbyz	17	0.992	1.00	-27.7	55.25	7.62	6.78
Dbzx	14	1.019	1.02	-44.0	41.17	7.56	5.28
Dbzy	12	0.996	1.00	-27.5	41.37	7.52	5.72
Dbzz	11	1.001	1.01	-25.1	39.48	7.71	6.46

Table 1: Inversion output parameters for Grids Aa-Da

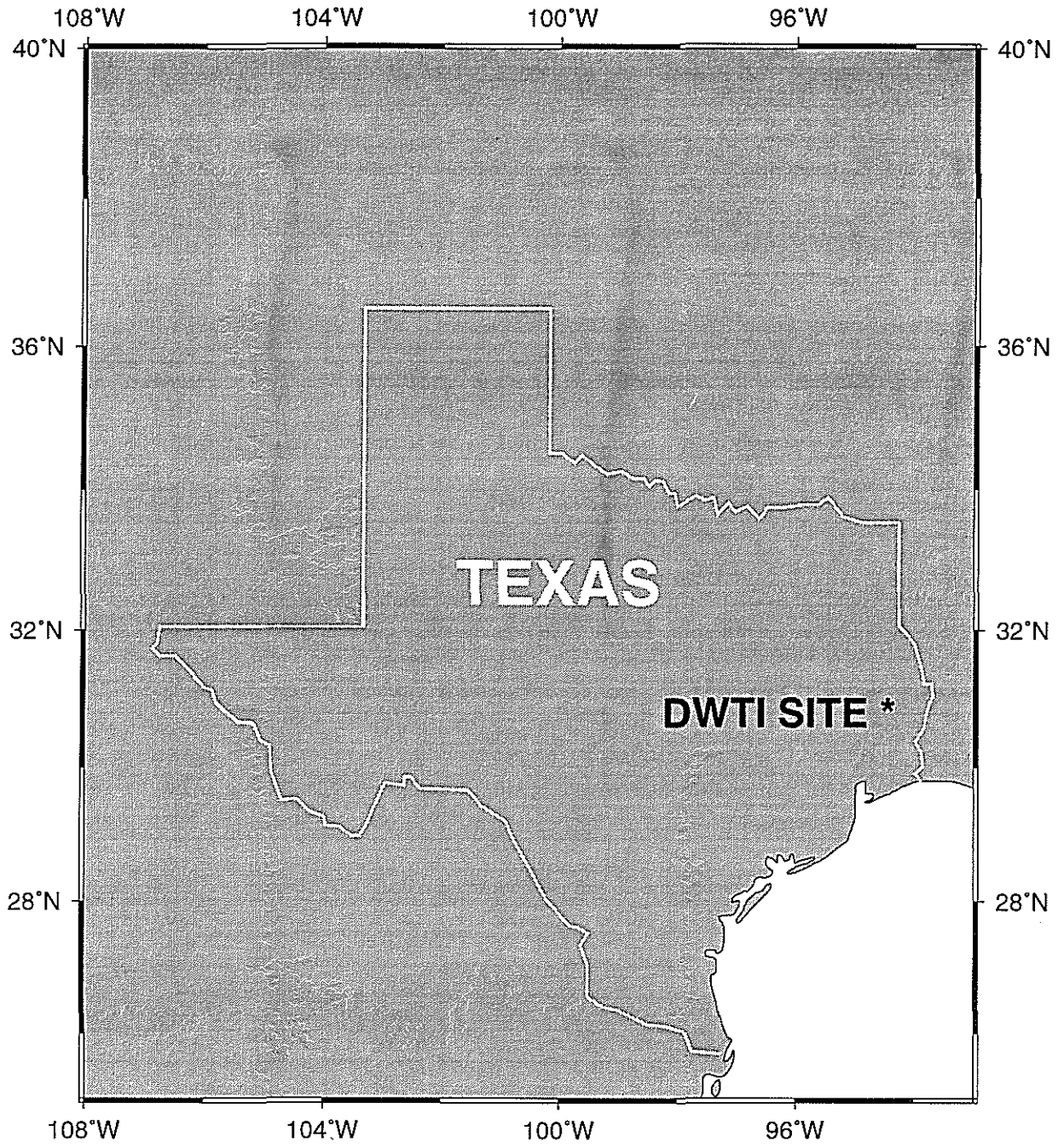

Figure 1: Regional location map of the Deep Well Treatment and Injection Site (DWTI) in Jasper, Texas.

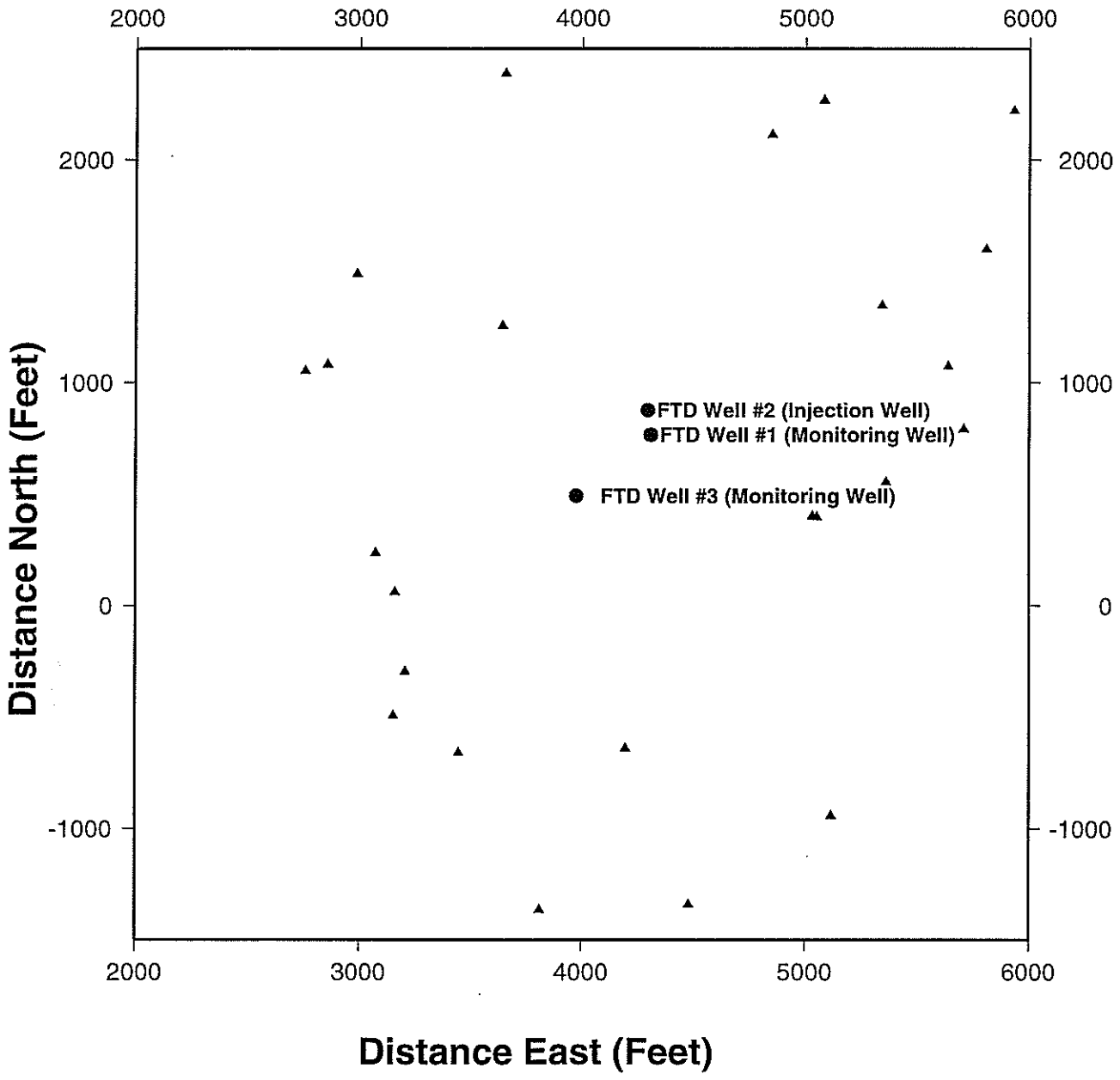

Figure 2: Site map of the DWTI Site indicating the locations of the Field Technology Demonstration (FTD) wells and the tiltmeters (triangles).

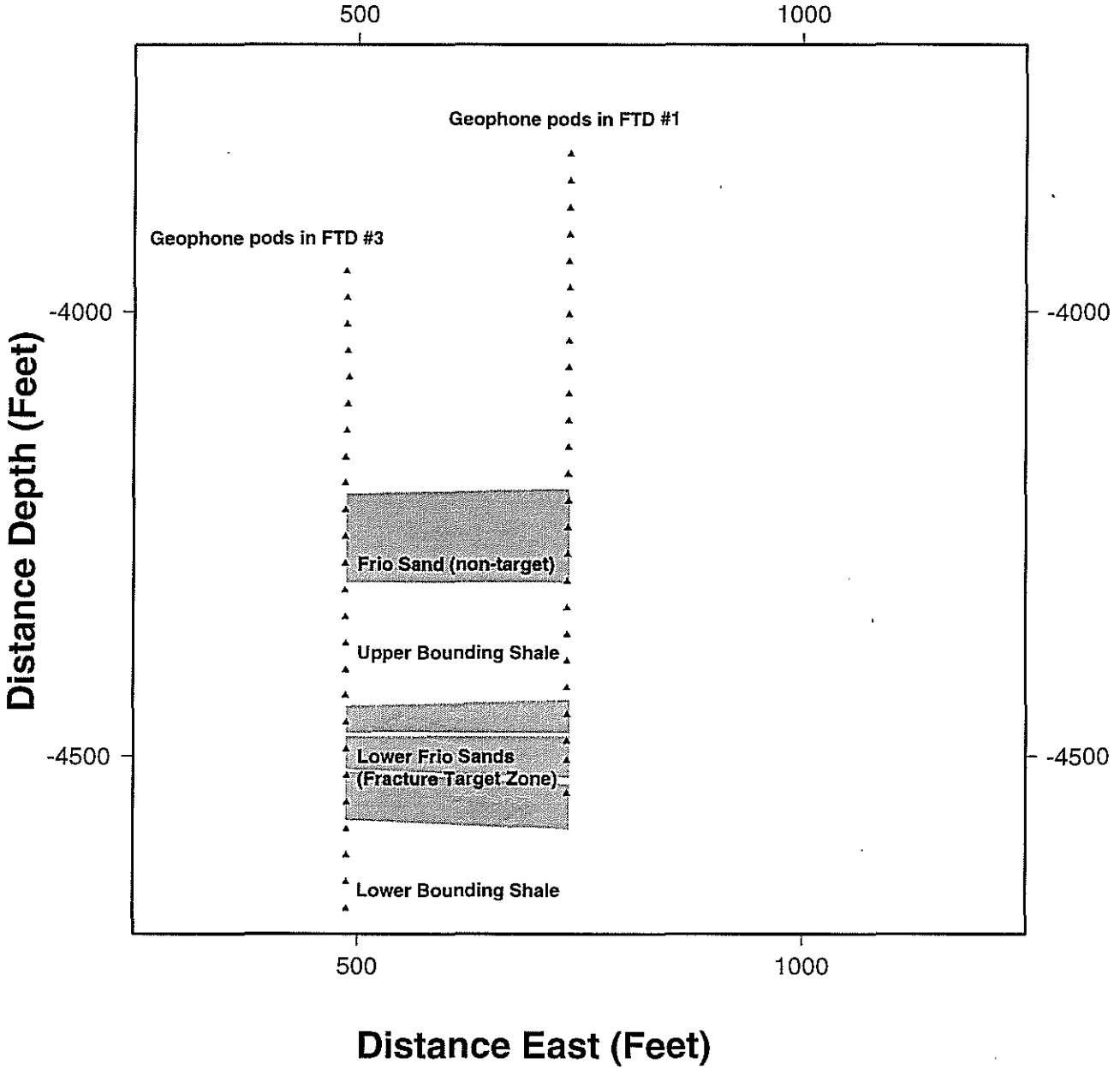

Figure 3: Cross-section of the DWTI monitoring wells indicating the locations of the FTD wells, geophones (triangles) and lithologic units.

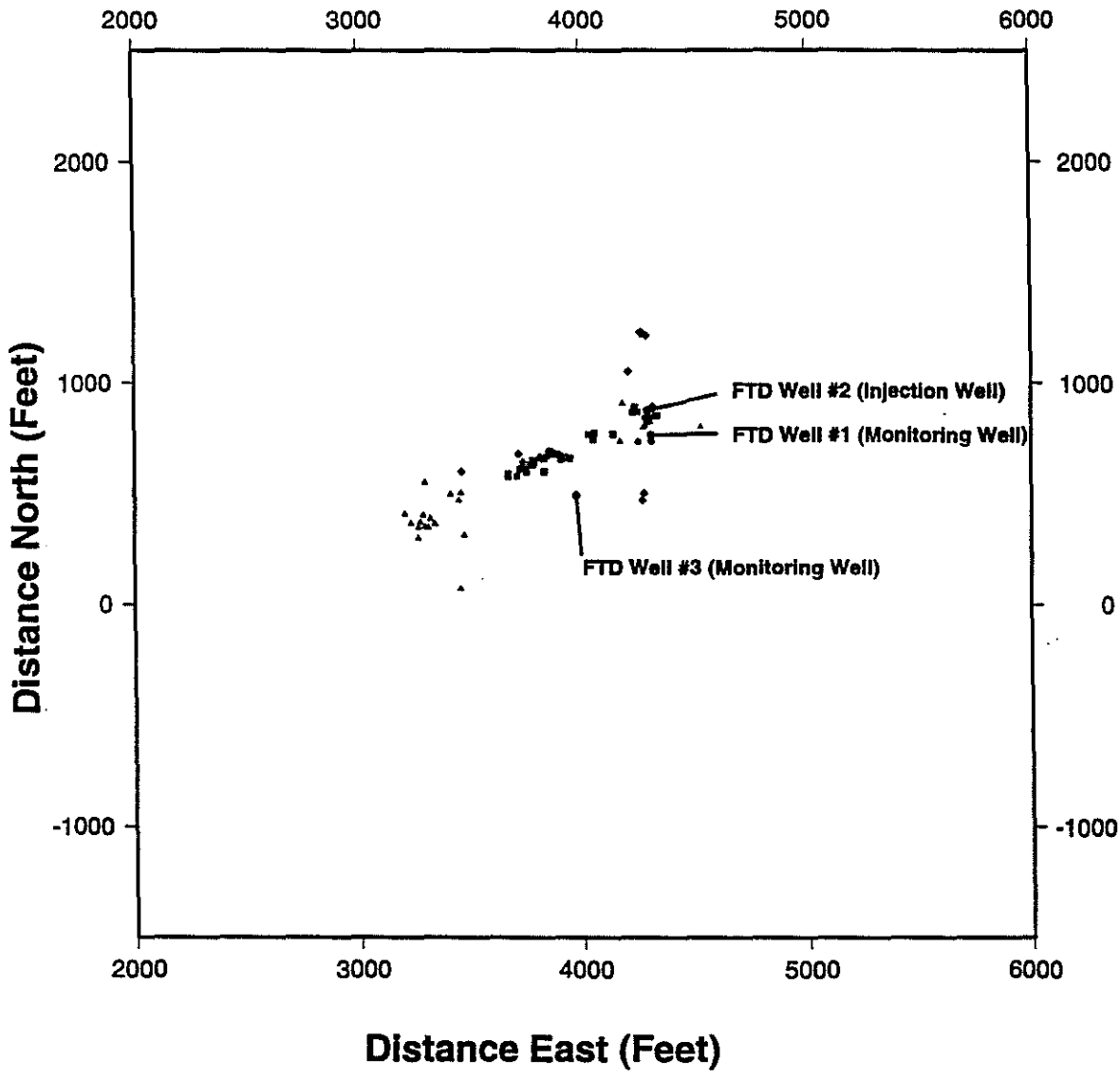

Figure 4: Epicentral locations of the 100 largest microseismic events, as located by ARCO (small circles=cycle 0, squares=cycle 1, triangles=cycle 2, diamonds=cycle3).

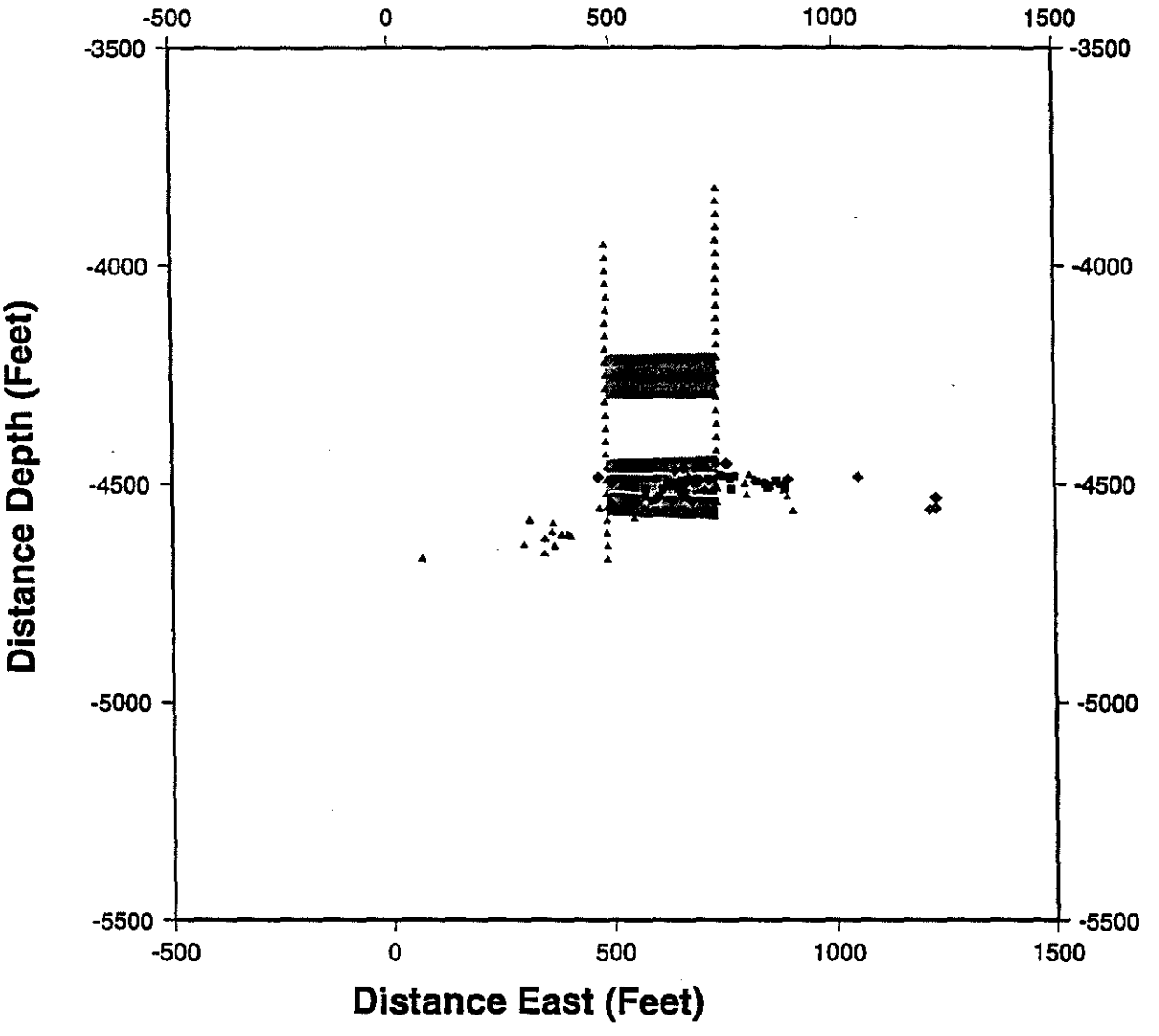

Figure 5: North-looking depth locations of the 100 largest microseismic events (small circles=cycle 0, squares=cycle 1, triangles=cycle 2, diamonds=cycle3).

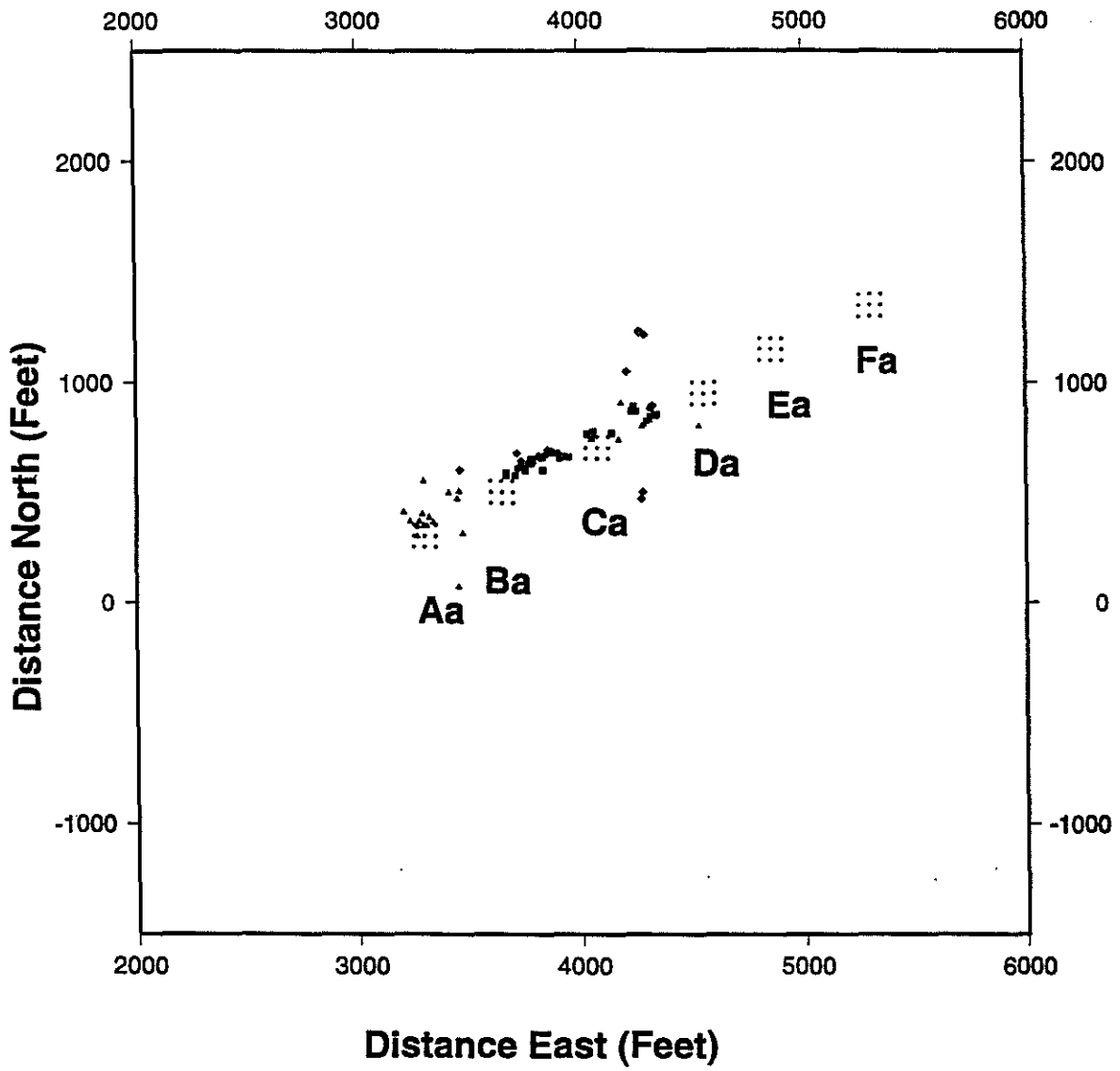

Figure 6: Synthetic microseismic event hypocenter grids Aa through Fa.

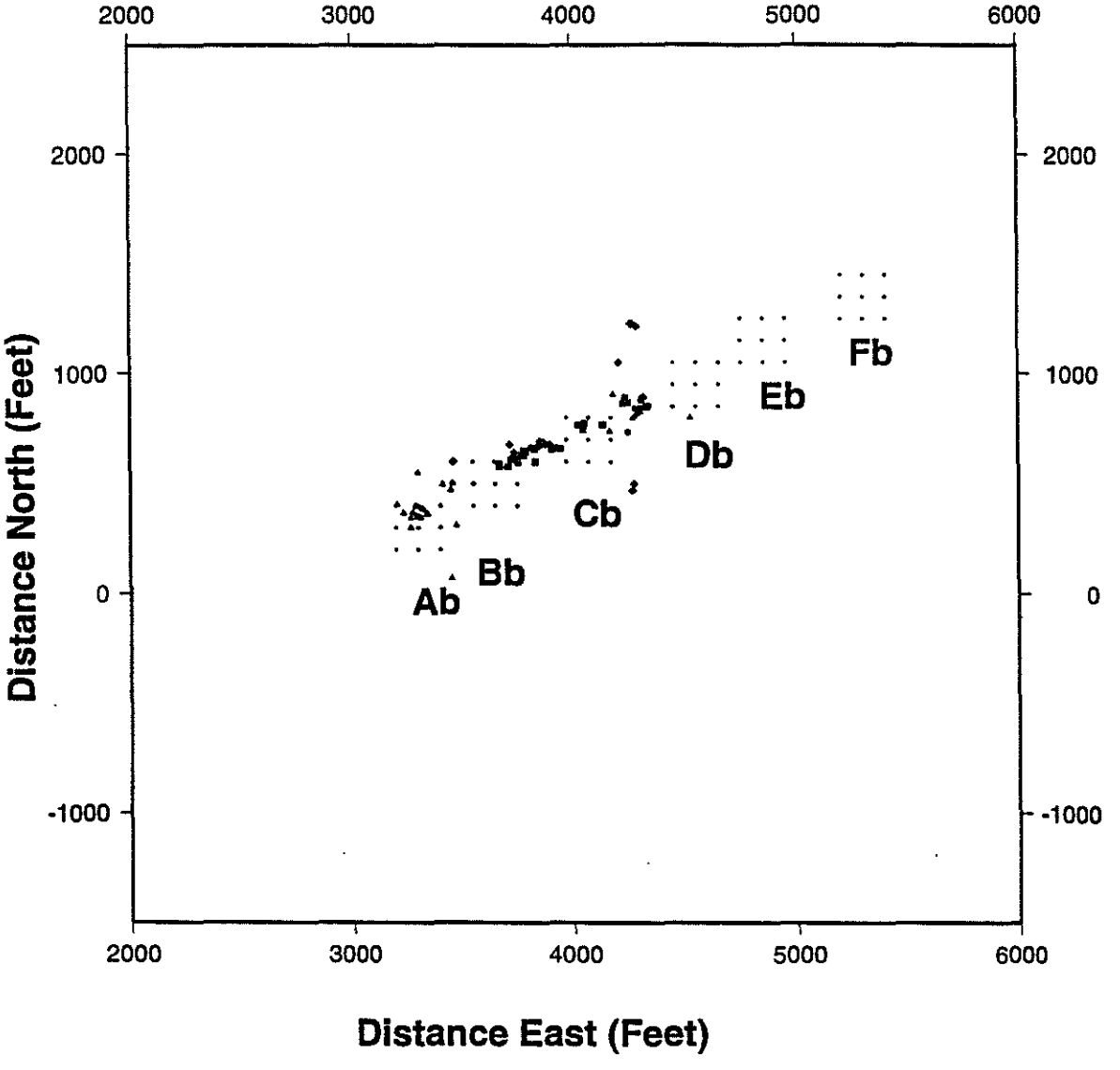

Figure 7: Synthetic microseismic event hypocenter grids Ab through Fb.

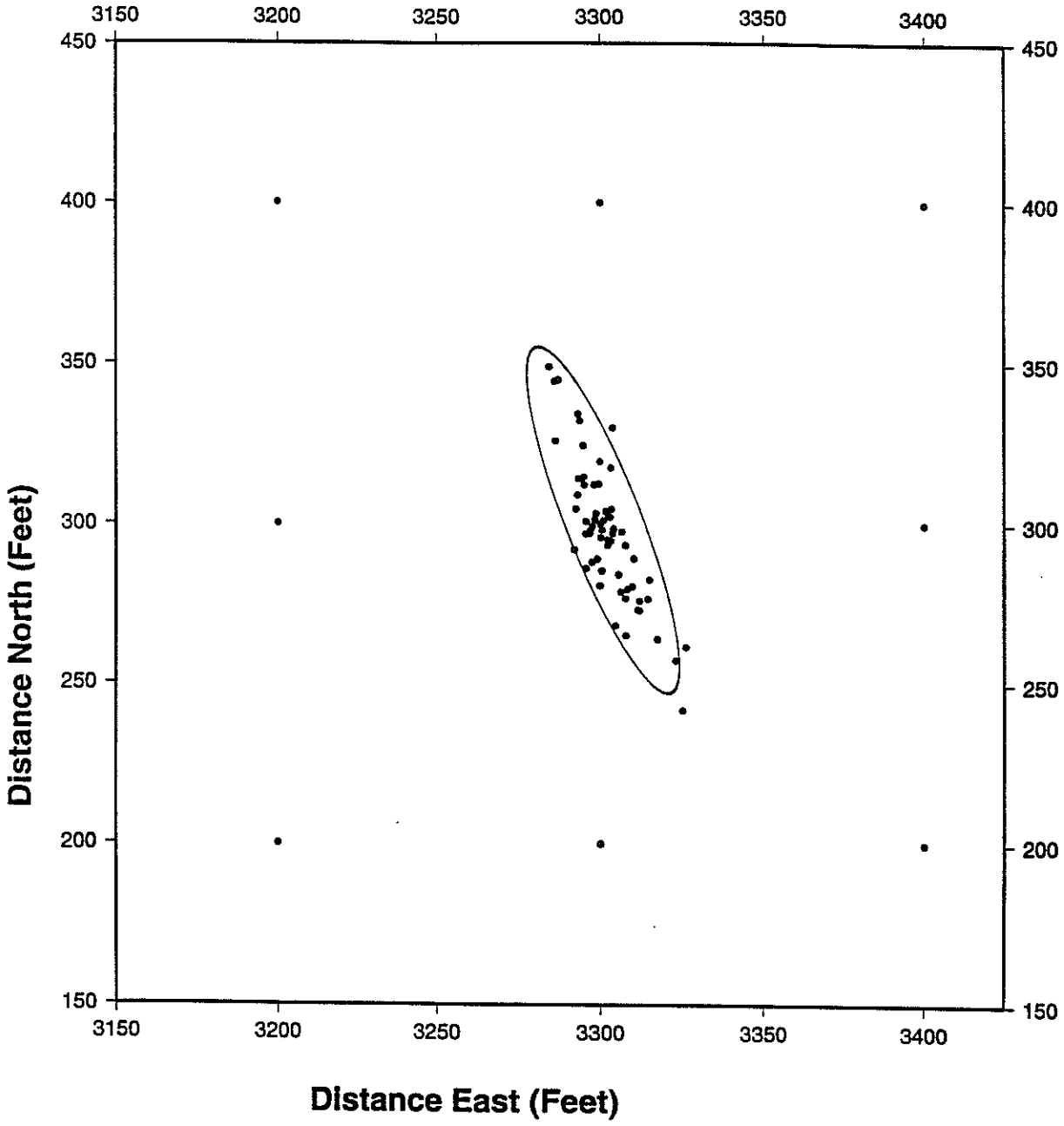

Figure 8: Predicted epicenters for event Abyy recalculated 60 times. (Triangles=real events from cycle 2.)

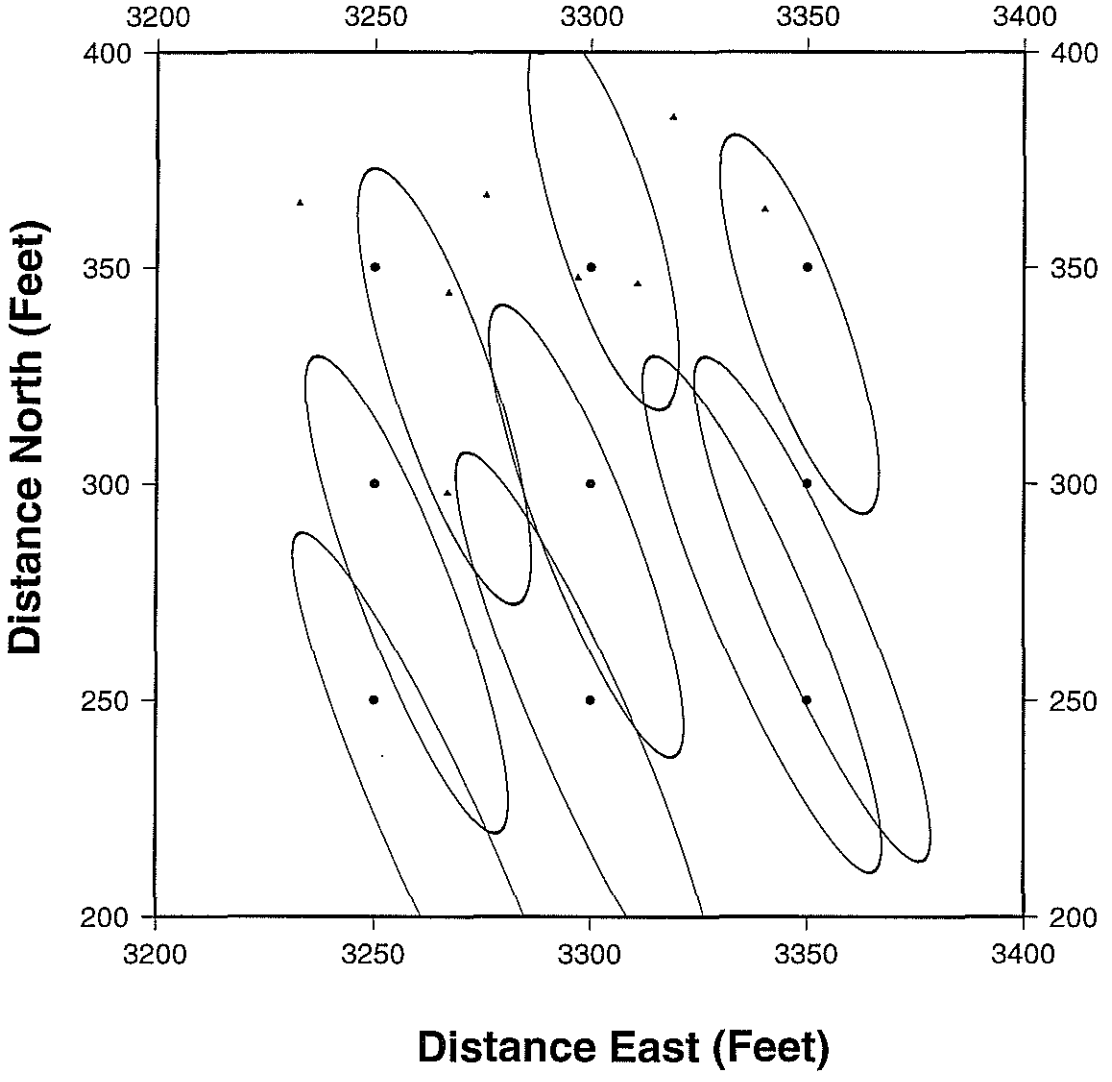

Figure 9: Projections of the absolute location 90% confidence regions for nine events from grid Aa. (Triangles=real events from cycle 2.)

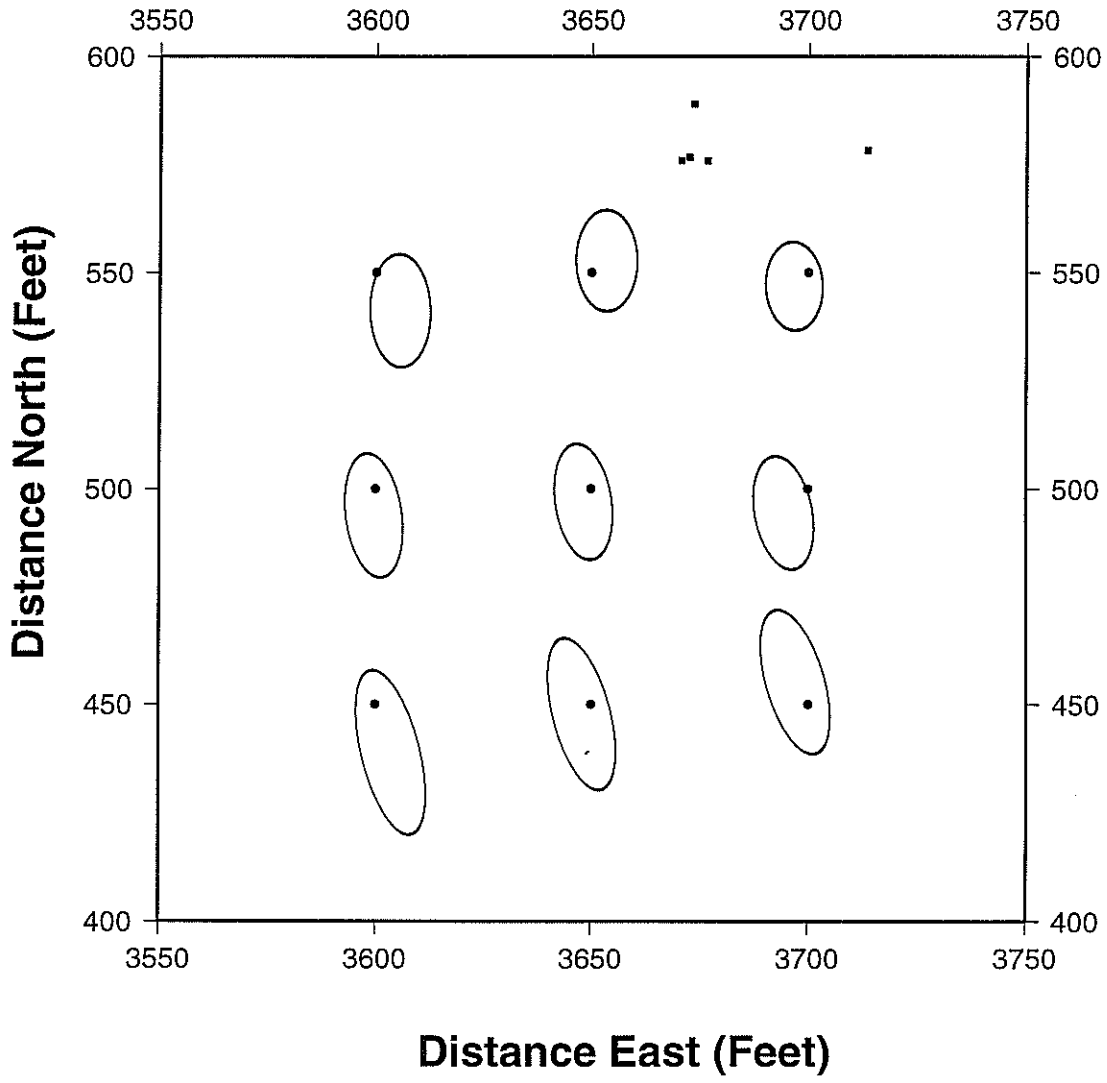

Figure 10: Projections of the absolute location 90% confidence regions for nine events from grid Ba. (Squares=real events from cycle 1.)

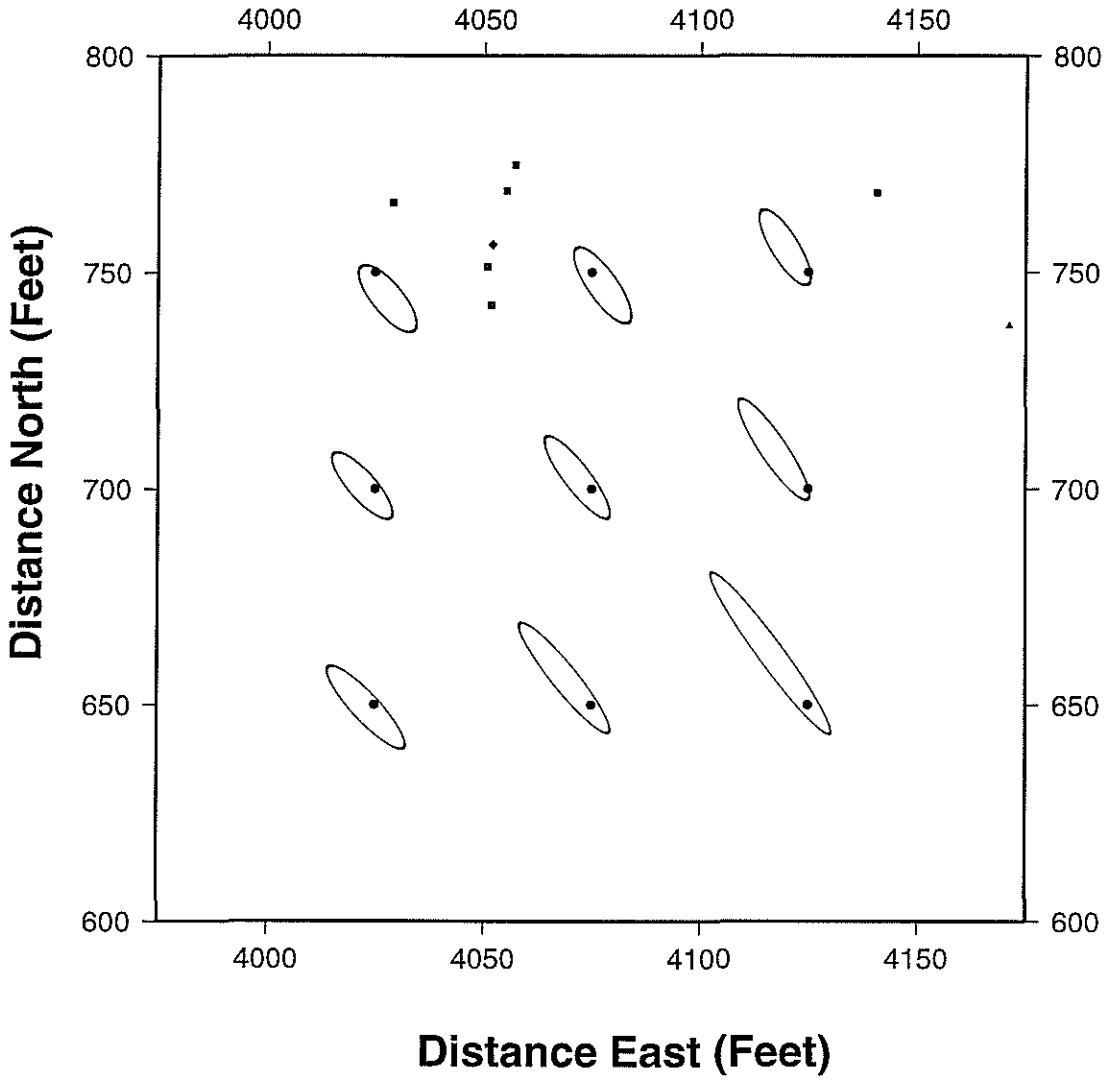

Figure 11: Projections of the absolute location 90% confidence regions for nine events from grid Ca. (Squares=real events from cycle 1, diamonds=real events from cycle 3.)

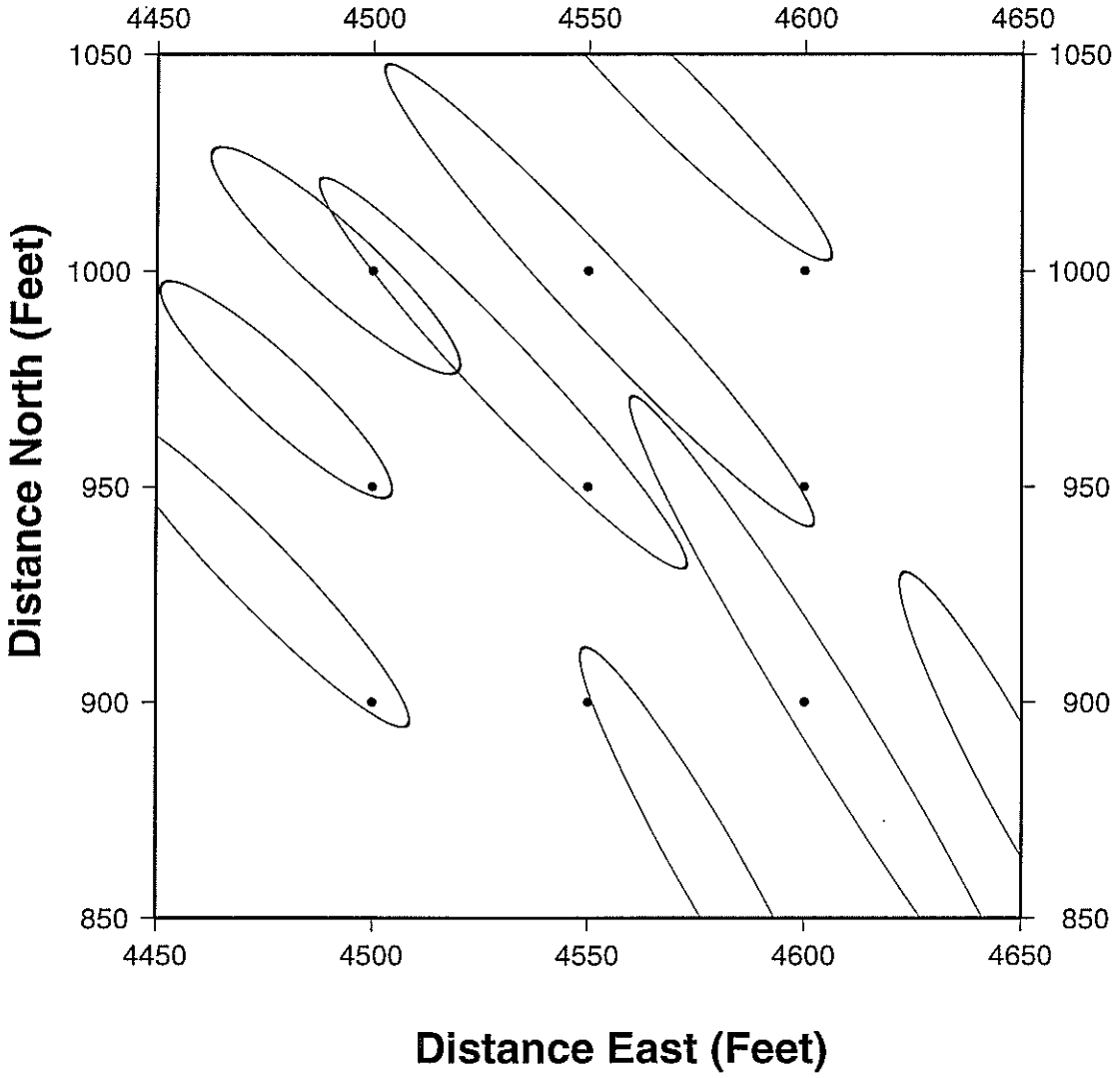

Figure 12: Projections of the absolute location 90% confidence regions for nine events from grid Da.

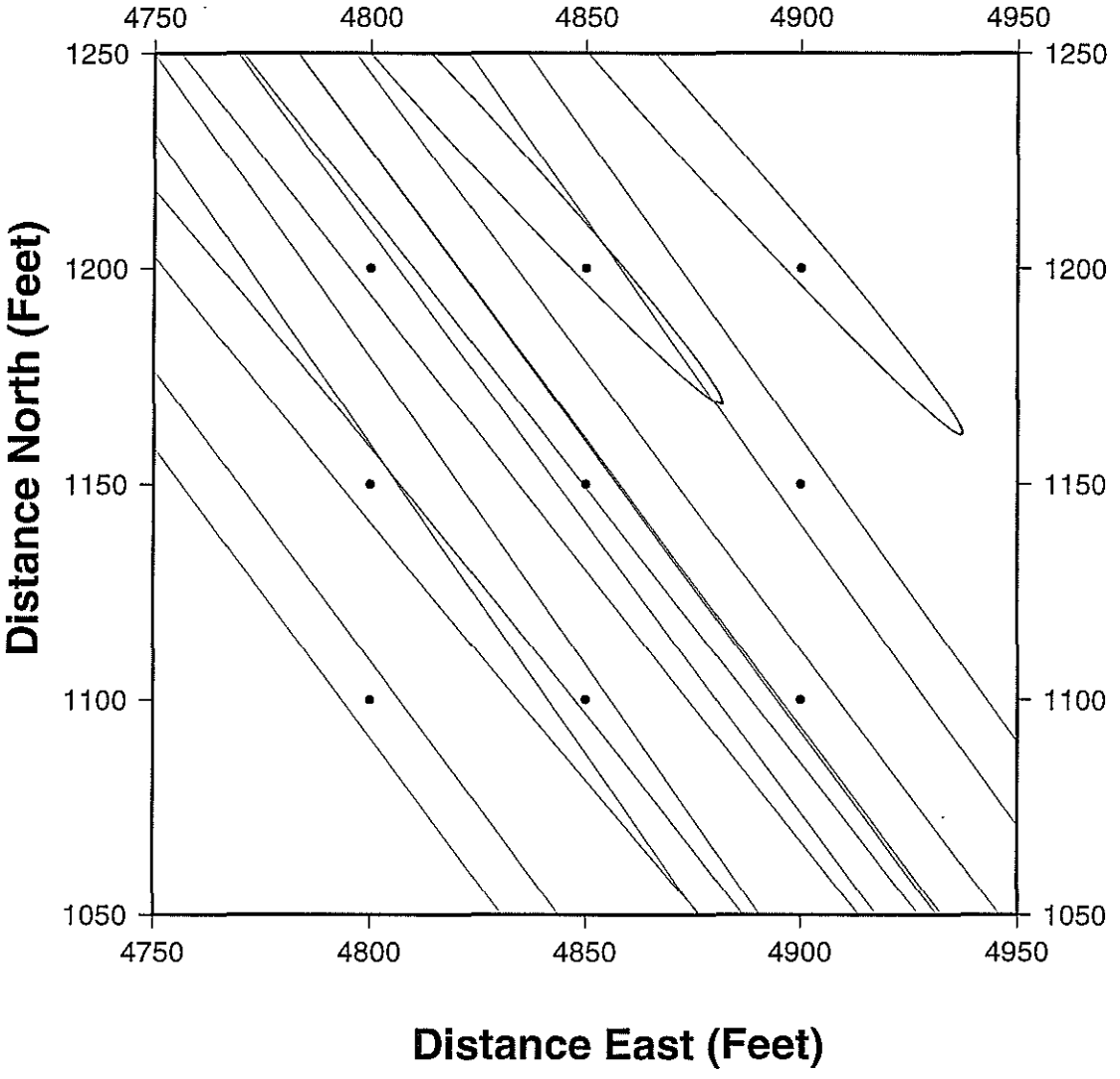

Figure 13: Projections of the absolute location 90% confidence regions for nine events from grid Ea. (Triangles=real events from cycle 2.)

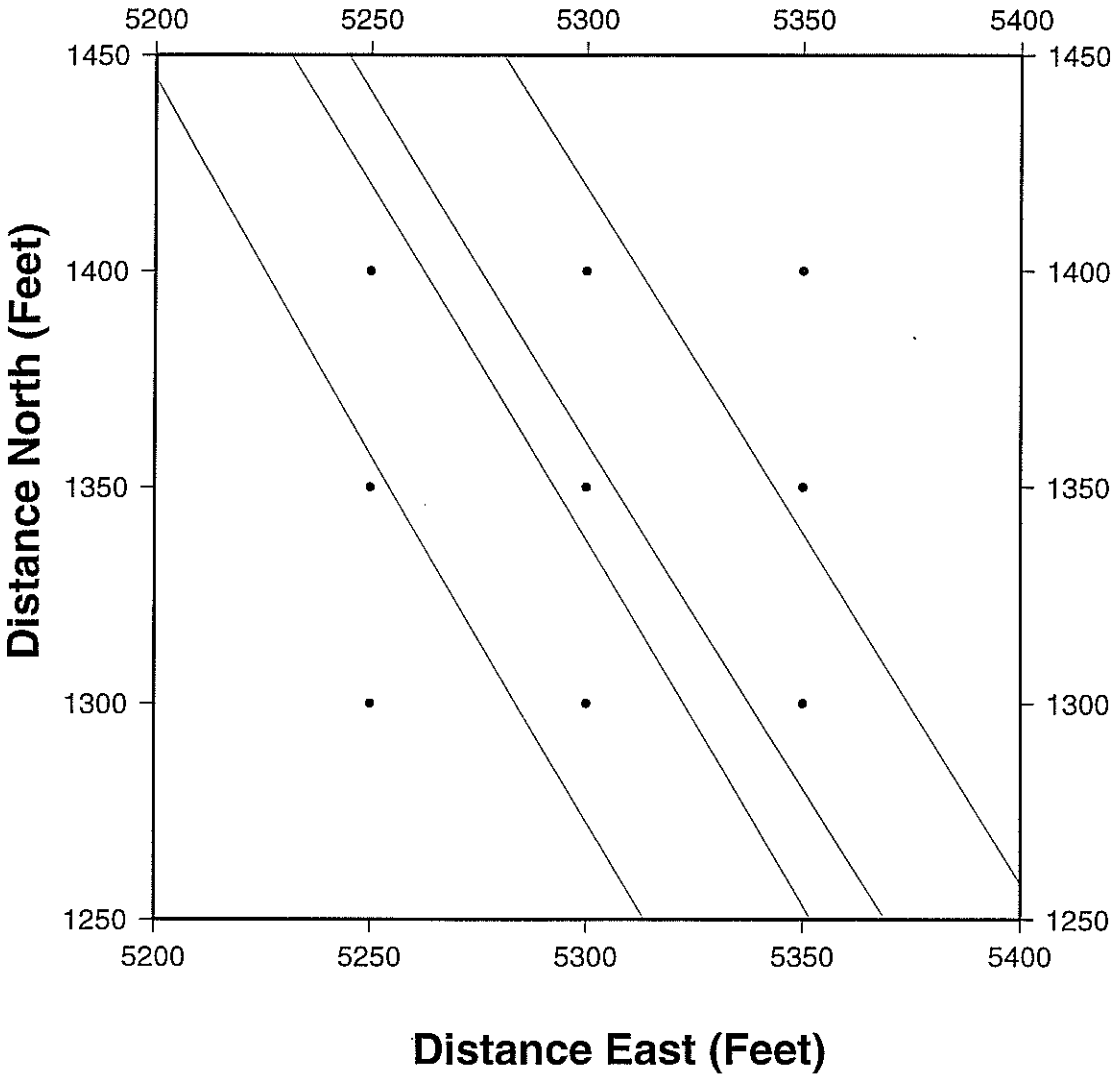

Figure 14: Projections of the absolute location 90% confidence regions for nine events from grid Fa. (Triangles=real events from cycle 2.)

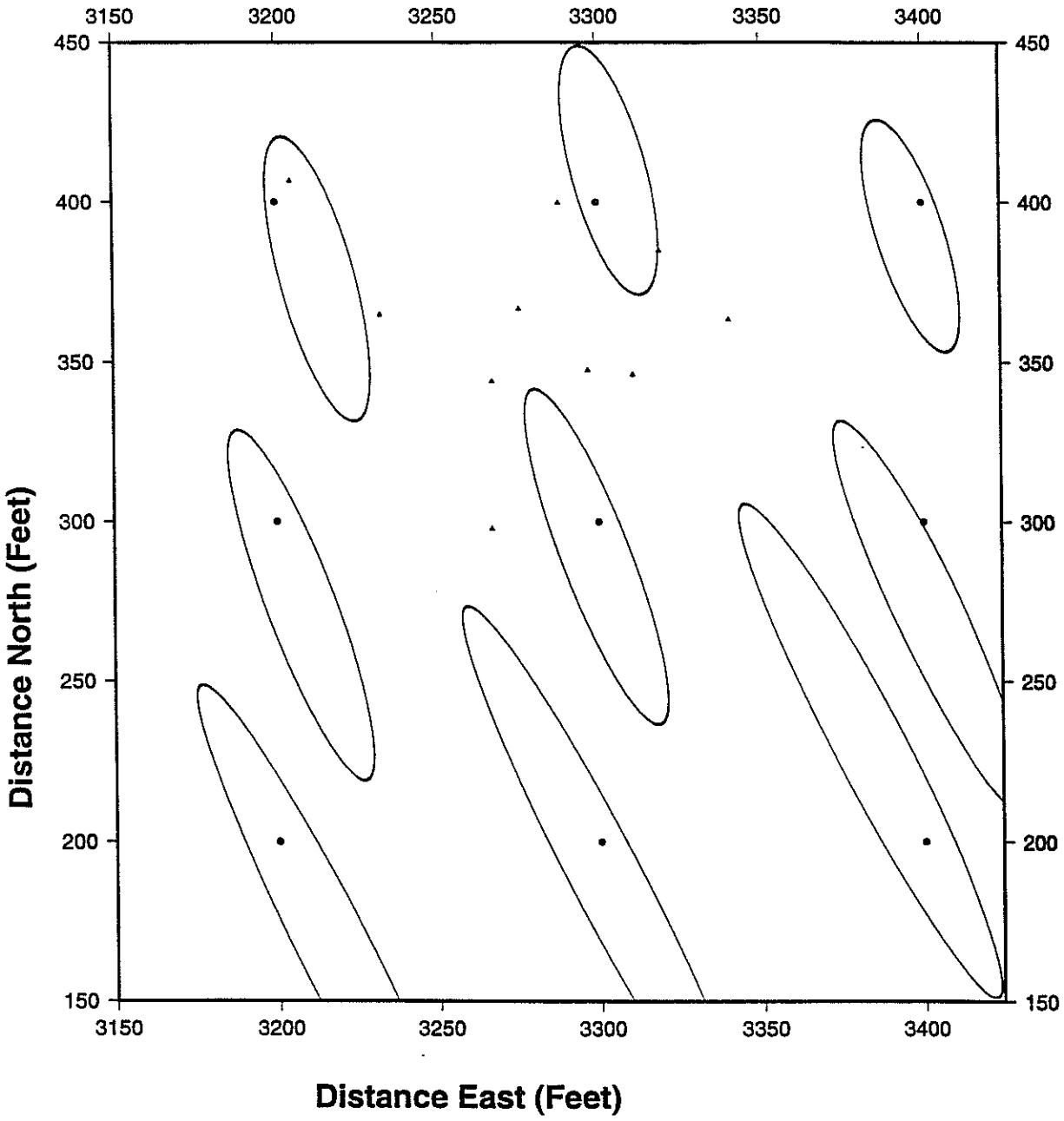

Figure 15: Projections of the absolute location 90% confidence regions for nine events from grid Ab. (Triangles=real events from cycle 2.)

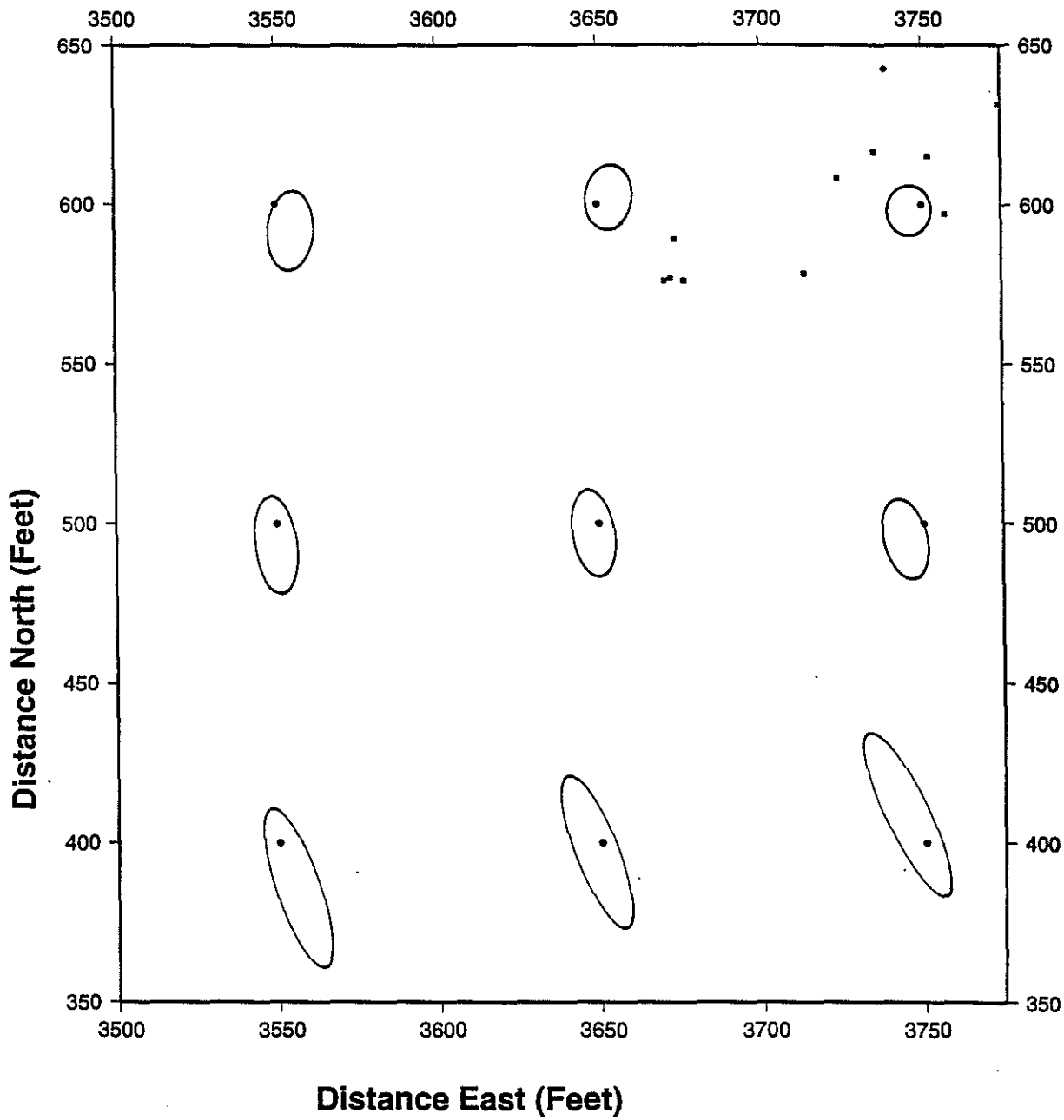

Figure 16: Projections of the absolute location 90% confidence regions for nine events from grid Bb. (Squares=real events from cycle 1.)

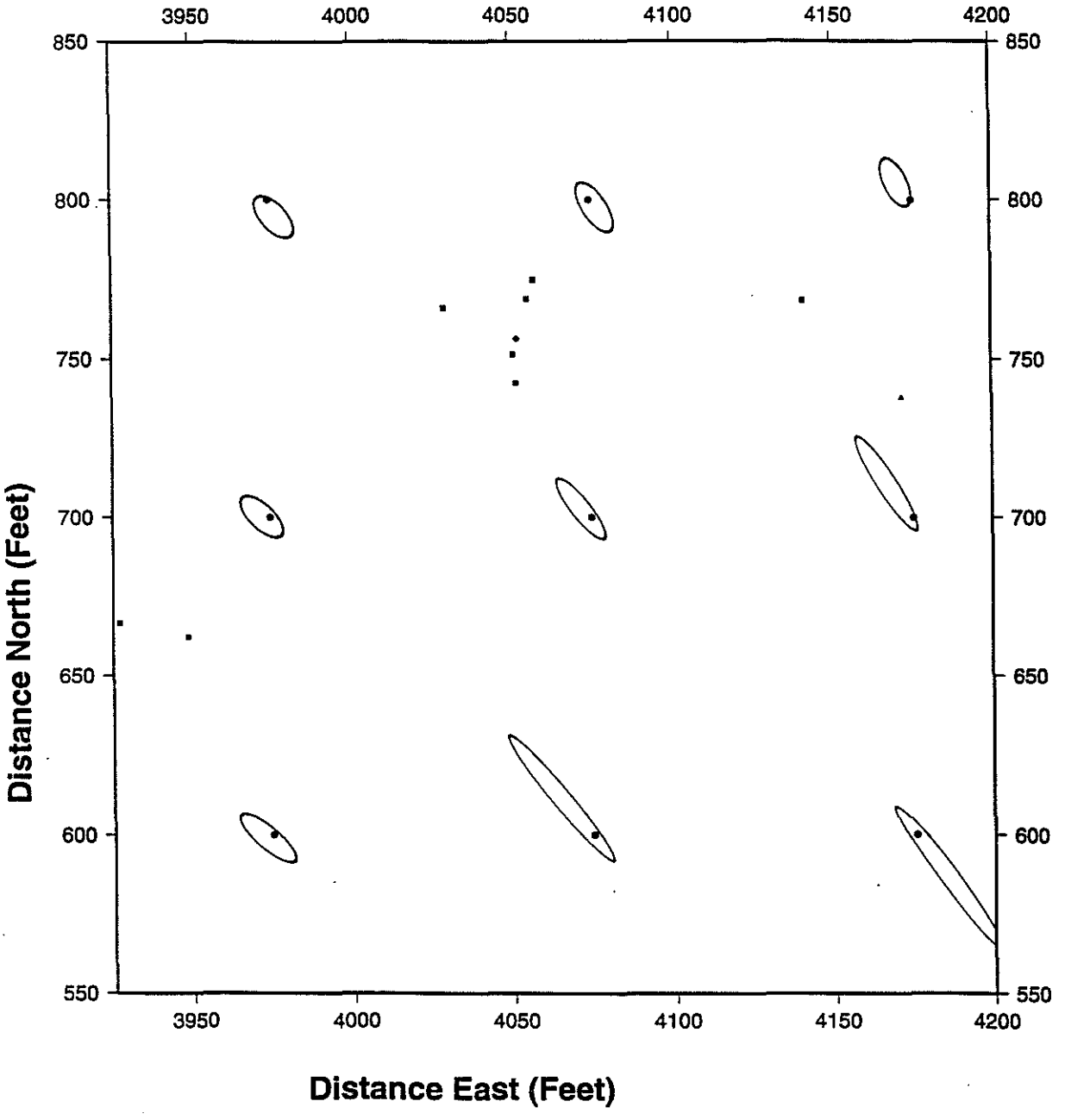

Figure 17: Projections of the absolute location 90% confidence regions for nine events from grid Cb.